

## The CMC-MRB Global Environmental Multiscale (GEM) Model. Part III: Nonhydrostatic Formulation

KAO-SAN YEH\*

*Centre de Recherche en Calcul Appliqué, Montréal, Québec, Canada*

JEAN CÔTÉ AND SYLVIE GRAVEL

*Meteorological Research Branch, Meteorological Service of Canada, Dorval, Québec, Canada*

ANDRÉ MÉTHOT AND ALAINE PATOINE

*Canadian Meteorological Centre, Meteorological Service of Canada, Dorval, Québec, Canada*

MICHEL ROCH AND ANDREW STANIFORTH<sup>+</sup>

*Meteorological Research Branch, Meteorological Service of Canada, Dorval, Québec, Canada*

(Manuscript received 8 August 2000, in final form 10 July 2001)

### ABSTRACT

An integrated forecasting and data assimilation system has been and is continuing to be developed by the Meteorological Research Branch (MRB) in partnership with the Canadian Meteorological Centre (CMC) of Environment Canada. Part III of this series of papers presents the nonhydrostatic formulation and some sample results. The nonhydrostatic formulation uses Laprise's hydrostatic pressure as the basis for its vertical coordinate. This allows the departure from the hydrostatic formulation to be incorporated in an efficient switch-controlled perturbative manner. The time discretization of the model dynamics is (almost) fully implicit semi-Lagrangian, where all terms including the nonlinear terms are (quasi-) centered in time. The spatial discretization for the adjustment step employs a staggered Arakawa C grid that is spatially offset by half a mesh length in the meridional direction with respect to that employed in previous model formulations. It is accurate to second order, whereas the interpolations for the semi-Lagrangian advection are of fourth-order accuracy except for the trajectory estimation. The resulting set of nonlinear equations is solved iteratively using a motionless isothermal reference state that gives the usual semi-implicit problem as a preconditioner. The Helmholtz problem that needs to be solved at each iteration is vertically separable, the impact of nonhydrostatic terms being simply a renormalization of the separation constants. The convergence of this iterative scheme is not greatly modified by the nonhydrostatic perturbation. Three numerical experiments are presented to illustrate the model's performance. The first is a test to show that hydrostatic balance at low resolution is well maintained. The second one is a mild orographic windstorm case, where the flow should remain hydrostatic, to test that hydrostatic balance at high resolution is also well maintained. The third one is a convective case taken from the Verification of the Origins of Rotation in Tornadoes Experiment (VORTEX). Although these results are encouraging, rigorous testing of the model's performance for strongly nonhydrostatic flows still remains to be done.

### 1. Introduction

The hydrostatic assumption, namely, the neglect of vertical acceleration in the vertical momentum equation

---

\* Current affiliation: Earth System Science Interdisciplinary Center, University of Maryland, College Park, Maryland.

<sup>+</sup> Current affiliation: Met Office, Bracknell, Berkshire, United Kingdom.

---

*Corresponding author address:* Dr. Andrew Staniforth, Dynamics Research Branch Head, Met Office, London Road, Bracknell, Berkshire RG12 2SZ, United Kingdom.  
E-mail: andrew.staniforth@metoffice.com

of the primitive equations, is an excellent approximation that is well respected in the atmosphere down to scales of 10 km or so. However, at these scales the dynamical effects excluded by the hydrostatic assumption, for example, internal wave breaking and overturning, start to become nonnegligible.

To date, computer limitations have been such that almost all operational weather forecast (and climate simulation) models have been run with horizontal mesh lengths coarse enough to confidently employ the hydrostatic primitive equations. Looking to the future however, this will change (Daley 1988). In particular, if a model is to be applied with meso- $\gamma$ -scale mesh

configurations, then it should use the fully compressible *nonhydrostatic* primitive equations instead of the so-called hydrostatic primitive ones. This motivates the use of “hydrostatic pressure” as the basis for a vertical coordinate as proposed in Laprise (1992). This coordinate system permits a switch-controlled choice between the hydrostatic primitive equations (for large- and synoptic-scale applications), and the nonhydrostatic primitive equations (for smaller-scale applications). The computational and memory overhead associated with the latter option can then be avoided for applications where the hydrostatic approximation is valid. A terrain-following normalized pressure version (Phillips 1957; Kasahara 1974) is possible (Bubnova et al. 1994, 1995), allowing an easy incorporation of the lower boundary, and a relaxation toward the horizontal upward from the earth’s surface. For atmospheric applications, there is virtually no scale restriction on using hydrostatic pressure as vertical coordinate since it only requires density to be positive; integrations are presented in Bubnova et al. (1995) with horizontal resolution as high as 80 m. Note however that terrain-following transformations ultimately break down in the presence of cliffs due to a breakdown of differentiability.

The model formulation presented here was outlined in Côté et al. (1994). It differs from the Bubnova et al. (1994, 1995) formulation in several aspects besides the horizontal discretization. First, the set of equations used is different: Laprise (1992) gave various alternative formulations, the subset chosen here is the minimal one having as supplementary equations the vertical equation of motion and the definition of vertical velocity (see section 2a). Second, the present dynamical formulation is (quasi-) centered (almost) fully implicit (see section 2c), whereas the Bubnova et al. (1995) one is (quasi-) centered semi-implicit: furthermore, the present formulation was developed for a new model with no constraint on being compatible with another model or system. The present formulation can be summarized as follows: minimal and simplest equation set, (almost) fully implicit (quasi-) centered time discretization, space discretization with consistent treatment of right- and left-hand-sides of the governing equations, algebraic elimination to derive the Helmholtz problem, and consistent backsubstitution.

## 2. Formulation

### a. Hydrostatic pressure and vertical coordinate

The “hydrostatic pressure” (denoted  $\pi$ ) of Laprise (1992) is defined as a pressure field in hydrostatic balance with  $\phi$ , the geopotential height. Thus

$$\frac{\partial \pi}{\partial \phi} = -\rho, \quad (2.1a)$$

where  $\rho$  is the density. Equation (2.1a) defines  $\pi$  to within an arbitrary additive horizontal field. The am-

biguity is lifted by further requiring that hydrostatic pressure and pressure be equal at the top of the model, taken here to be at constant pressure  $\pi_T$ . Full pressure ( $p$ ) is then represented in the model as a perturbation from  $\pi$ , and so

$$p = \pi \exp(q') \Rightarrow \ln p = \ln \pi + q', \quad q'_T = 0, \quad (2.1b)$$

where subscript  $T$  denotes evaluation at the model top and primes denote a perturbation quantity. In the hydrostatic limit hydrostatic pressure and full pressure become identical, and a measure of departure from hydrostatic balance is defined by

$$\mu \equiv \frac{\partial p}{\partial \pi} - 1, \quad (2.2)$$

referred to herein as the nonhydrostatic index.

Since  $\rho$  is strictly positive,  $\pi$  varies monotonically with height and can be used to define a terrain-following vertical coordinate:

$$\eta \equiv \frac{\pi - \pi_T}{\pi_S - \pi_T}, \quad (2.3)$$

where  $\pi_S = \pi_S(\lambda, \theta)$  and the subscripts S and T respectively, refer to evaluation at the surface and at the top of the model.

To allow for a more general nonlinear relationship between  $\eta$  and  $\pi$  than (2.3), and to keep a quasi-invariant formulation with little dependence on the exact form of the relationship, the terrain-following vertical coordinate of the model, denoted by  $Z$ , is taken to be  $\pi^*(\eta)$ , the reference pressure profile. It is a monotonic function of  $\eta$ , which is obtained from  $\eta(\pi, \pi_S, \pi_T)$  by replacing the fields  $\pi$ ,  $\pi_S$ , and  $\pi_T$  by their reference values  $Z \equiv \pi^*$ ,  $Z_S \equiv \pi_S^*$ , and  $Z_T \equiv \pi_T^*$  respectively. Thus, for the particular linear case (2.3),

$$\frac{Z - Z_T}{Z_S - Z_T} = \frac{\pi - \pi_T}{\pi_S - \pi_T} \quad (\equiv \eta). \quad (2.4)$$

The reference or basic state is motionless and isothermal with temperature  $T^*$ . The reference potential temperature  $\theta^*$  and geopotential  $\phi^*$ , respectively, are therefore

$$\theta^* = T^* \left( \frac{Z}{p_{00}} \right)^{-\kappa}, \quad \phi^* = -R_d T^* \ln \left( \frac{Z}{Z_S} \right), \quad (2.5)$$

where  $\kappa = R_d/c_{pd}$ ,  $R_d$  is the gas constant for dry air,  $c_{pd}$  is the specific heat of dry air at constant pressure, and  $p_{00} \equiv 1015$  hPa is a constant pressure.

Note that since the time discretization of the model is (almost) fully implicit (see section 2c below), the basic-state parameters are simply relaxation parameters, which are chosen to accelerate the convergence of the iterative scheme and ensure the stability of the model.

### b. Governing equations

The governing equations are the forced *nonhydrostatic* primitive equations:

$$\frac{d\mathbf{V}^H}{dt} + R_d T_v \nabla \ln p + (1 + \mu) \nabla \phi + f(\mathbf{k} \times \mathbf{V}^H) = \mathbf{F}^H, \quad (2.6)$$

$$\frac{ds}{st} + D + \frac{\partial \dot{Z}}{\partial Z} = 0, \quad (2.7)$$

$$\begin{aligned} \frac{d \ln \theta}{dt} &\equiv \frac{d}{dt} \ln \left( \frac{\theta}{\theta^*} \right) + \dot{Z} \frac{d}{dZ} \ln \theta^* \\ &\equiv \frac{d}{dt} \left[ \ln \left( \frac{T_v}{T^*} \right) - \kappa \ln \left( \frac{p}{Z} \right) \right] - \frac{\kappa \dot{Z}}{Z} = F^\theta, \end{aligned} \quad (2.8)$$

$$\delta_H \frac{dw}{dt} - \mu g = \delta_H F^v, \quad (2.9)$$

$$\frac{d\phi}{dt} - gw = \frac{d(\phi - \phi^*)}{dt} - R_d T^* \frac{\dot{Z}}{Z} - gw = 0, \quad (2.10)$$

$$\frac{dq_v}{dt} = F^{q_v}, \quad (2.11)$$

$$\frac{\partial \phi}{\partial Z} = -\frac{1}{\rho} \frac{\partial \pi}{\partial Z}, \quad (2.12)$$

$$p = \rho R_d T_v, \quad (2.13)$$

where

$$\dot{Z} \equiv \frac{dZ}{dt}, \quad \text{and} \quad \frac{d}{dt} \equiv \frac{\partial}{\partial t} + \mathbf{V}^H \cdot \nabla + \dot{Z} \frac{\partial}{\partial Z}, \quad (2.14)$$

is the substantive derivative following the fluid. Here,  $\mathbf{V}^H$  is horizontal velocity,  $D$  is horizontal divergence,  $T_v$  is virtual temperature,  $s \equiv \ln(\partial \pi / \partial Z) = \ln[(\pi_s - \pi_T) / (Z_s - Z_T)]$  is the mass variable and depends only on the horizontal,  $q_v$  is specific humidity of water vapor,  $f$  is the Coriolis parameter,  $\mathbf{k}$  is a unit vector along the rotation axis of the earth,  $g$  is the vertical acceleration due to gravity, and  $\mathbf{F}^H$ ,  $F^\theta$ ,  $F^v$ , and  $F^{q_v}$  are parameterized physical forcings. Equations (2.6)–(2.12) are, respectively, the horizontal momentum, continuity, thermodynamic, vertical momentum, vertical velocity, moisture, and hydrostatic equations, and (2.13) is the equation of state, taken here to be the ideal gas law. A hydrostatic/nonhydrostatic switch  $\delta_H$  has been introduced into (2.9). When  $\delta_H = 0$ , (2.9) reduces to  $\mu = 0$ . This implies that  $\pi \equiv p$  from (2.1b) and (2.2), that (2.10) decouples completely, and that the governing equations then revert to the usual hydrostatic primitive equation set. When  $\delta_H = 1$ , the original nonhydrostatic set is recovered. Thus this set (see Tanguay et al. 1990) only differs from the hydrostatic primitive equations by the inclusion of the vertical acceleration term  $dw/dt$ .

The boundary conditions are the same for both the nonhydrostatic and hydrostatic sets: periodicity in the horizontal, and no motion across the top and bottom of the atmosphere. Thus

$$\dot{Z} = 0 \text{ at } Z = Z_s \text{ and } Z_T. \quad (2.15)$$

### c. Temporal discretization

The time discretization is the same as in Côté et al. (1998b), and only the essential elements for what follows are recalled here. Equations (2.6)–(2.12) are first integrated in the absence of forcing, and the parameterized forcing terms appearing on the right-hand sides of (2.6)–(2.11) are then computed and added using the fractional-step time method (Yanenko 1971).

The time discretization used to integrate the frictionless adiabatic equations of the first step is (almost) fully implicit/semi-Lagrangian. ‘‘Fully implicit’’ refers here to the time discretization of (2.6)–(2.12) in the absence of the parameterized forcings. However these forcing terms are not treated fully implicitly but as a corrector to an adiabatic predictor and, as described at the end of this section, the trajectories are computed in a predictor–corrector manner. Thus the nomenclature ‘‘(almost) fully implicit’’ has been adopted to concisely summarize the time discretization.

Consider a prognostic equation of the form

$$\frac{dF}{dt} + G = 0. \quad (2.16)$$

Such an equation is approximated by time differences and weighted averages along a trajectory determined by an approximate solution to

$$\begin{aligned} \frac{d\mathbf{r}}{dt} &= \mathbf{V}^H(\mathbf{r}, Z, t), & \frac{d^2\mathbf{r}}{dt^2} &= -\mathbf{r} \left| \frac{\mathbf{V}^H}{a} \right|^2, \\ \frac{dZ}{dt} &= \dot{Z}(\mathbf{r}, Z, t), & \frac{d^2Z}{dt^2} &= 0, \end{aligned} \quad (2.17)$$

where  $\mathbf{r}(\lambda, \theta)$  is the position vector on the sphere of a fluid element and  $a$  is the (constant) radius of the earth. The vertical displacement is obtained neglecting acceleration, as is usual in semi-Lagrangian schemes, whereas for the horizontal displacement the motion is constrained to the sphere. Denoting by  $\mathbf{x}_3 = \{\mathbf{r}, Z\}$  the three-dimensional position vector, (2.16) is discretized as

$$\begin{aligned} &\frac{(F^n - F^{n-1})}{\Delta t} \\ &+ \left[ \left( \frac{1}{2} + \varepsilon \right) G^n + \left( \frac{1}{2} - \varepsilon \right) G^{n-1} \right] = 0, \end{aligned} \quad (2.18)$$

where  $\psi^n = \psi(\mathbf{x}_3, t)$ ,  $\psi^{n-1} = \psi[\mathbf{x}_3(t - \Delta t), t - \Delta t]$ ,  $\psi = \{F, G\}$ ,  $t = n\Delta t$ .

Note that this scheme is decentered along the trajectory, as in Rivest et al. (1994), to avoid the spurious resonant response arising from a centered approximation in the presence of orography. Cubic interpolation is used everywhere for upstream evaluations [cf. (2.18)] except for the trajectory computations [cf. (2.17)], where linear interpolation is used with no visible degradation in the results.

Grouping terms at the new time on the left-hand side

and known quantities on the right-hand side, (2.18) may be rewritten as

$$\frac{F^n}{\tau} + G^n = \frac{F^{n-1}}{\tau} - \left( \frac{1 - 2\varepsilon}{1 + 2\varepsilon} \right) G^{n-1} \equiv R^{n-1}, \quad (2.19)$$

where  $\tau \equiv (1 + 2\varepsilon)\Delta t/2$ . This yields the set of coupled nonlinear equations (B.1) of appendix B for the unknown quantities at the mesh points of a regular grid at the new time  $t$ , the solution of which is discussed in section 2e.

To ensure the stability of this implicit treatment, the trajectory equation (2.17) is solved in a predictor–corrector manner. This is done by first using the time-*extrapolated* 3D wind at time  $t - \Delta t/2$  to obtain a *predicted* estimate of the displacements [cf. (2.17)], and also of the solution. These are then *corrected* by using the time-*interpolated* wind at time  $t - \Delta t/2$  to obtain the final displacements and solution. Further iteration of this procedure is possible, albeit at some cost, but although available it has not to date been needed in practice—whether this will however be an issue for strongly nonhydrostatic flows remains to be seen.

#### d. Spatial discretization

The horizontal and vertical discretization are as in Côté et al. (1998b): a variable-resolution discretization on an Arakawa C grid is used in the horizontal with the supplementary fields related to the inclusion of nonhydrostatic effects located on the scalar grid. The essential elements of the spatial discretization are presented in appendix A. The discretization is centered almost everywhere and, hence, is almost everywhere of second order in space. The only exception is in the variable portion of the horizontal grid, where the computation of the horizontal divergence is not exactly centered, but as argued in Fox-Rabinovitz et al. (1997), for small uniform constant stretching the accuracy is still second order.

The accuracy of the spatial discretization can be verified by examining the spectra of the discrete operators of appendix A [cf. (A.16)–(A.17), (A.23)–(A.24)] and comparing them to those of the underlying continuous problems. In the  $\lambda$  direction, the generalized eigenvalue problem,

$$P_{\lambda\lambda}\Lambda_i = \varepsilon_i P(\lambda)\Lambda_i, \quad i = 1, \text{NI}, \quad (2.20)$$

is a discretization of the problem of finding the Fourier modes of period  $2\pi$ , and for a uniform grid the discrete modes are identical to the continuous modes except that the eigenvalues are different. The error on the eigenvalue corresponding to the modes of wavenumber  $m$  is

$$-m^2 + \left[ \left( \frac{2}{\Delta\lambda} \right) \sin\left( \frac{m\Delta\lambda}{2} \right) \right]^2 = -\frac{\pi^2 m^4}{3\text{NI}^2} + \text{HOT}, \quad (2.21)$$

where HOT denotes “higher-order terms” and is therefore of second-order accuracy.

Similarly in the  $\theta$  direction, the generalized eigenvalue problem,

$$P_{\theta\theta}\Theta_j = \varepsilon_j P(\theta)\Theta_j, \quad j = 1, \text{NJ}, \quad (2.22)$$

is a discretization of the problem of finding the Legendre polynomials (the zonal spherical harmonics), and the  $j$ th discrete eigenvalue should converge to  $-j(j - 1)$ . This is verified numerically for the third mode [ $P_2(\sin\theta)$ ]. The latitudes of the uniform grid are given by

$$\theta_j = \frac{(2j - \text{NJ} - 1)}{2\text{NJ}}\pi, \quad j = 1, \text{NJ}. \quad (2.23)$$

Fitting the form  $a\text{NJ}^b$  to the error computed with  $\text{NJ} = 51, 71, 91$ , and  $111$  respectively, yields  $a \approx -27.06$ ,  $b \approx -1.9994$ , thus numerically confirming the formal second-order accuracy.

In the  $Z$  direction, the generalized eigenvalue problem,

$$V_{ZZ}(\delta_H = 0)\Xi_k = \varepsilon_k V(Z)\Xi_k, \quad k = 1, \text{NK}, \quad (2.24)$$

is a discretization of the problem of finding the vertical structure functions for  $P$  [cf. (B.5)] of the normal modes of the linearized equations. The continuous problem is given by

$$\begin{aligned} L(L + 1)\Xi &= \mu\Xi, & L\Xi|_{z_T} &= 0, \\ (\kappa + L)\Xi|_{z_S} &= 0, \end{aligned} \quad (2.25)$$

where  $L \equiv \partial/\partial \ln Z$ . Equation (2.25) can be solved analytically and the eigenvalues ( $\mu$ ) are the roots of the transcendental equation:

$$\begin{aligned} \tan(lH) &= \frac{\kappa l}{l^2 + \frac{1}{4} - \frac{\kappa}{2}}, & H &= \ln\left(\frac{Z_S}{Z_T}\right), \\ l^2 &= -\mu - \frac{1}{4}. \end{aligned} \quad (2.26)$$

Taking  $Z_T = 10$  hPa,  $Z_S = 1000$  hPa, and  $\kappa = 0.285\,491\,217\,95$ , the first three roots are:

- 1)  $-0.218\,119\,108\,289\,177\,3$ ,
- 2)  $-0.811\,620\,026\,369\,796\,0$ , and
- 3)  $-2.225\,995\,779\,229\,059$ .

The convergence to the third eigenvalue is investigated numerically by successive refinement of the vertical grid:

$$Z_k = Z_S \exp\left[ -\frac{(\text{NK} - k)}{(\text{NK} - 1)}H \right], \quad k = 1, \text{NK}. \quad (2.27)$$

Fitting the form  $a(\text{NK} - 1)^b$  to the error computed with  $\text{NK} = 51, 71, 91$ , and  $111$ , respectively, yields  $a \approx 20.837$ ,  $b \approx -2.0018$ , again numerically confirming the formal second-order accuracy.

*e. Solving the coupled nonlinear set of discretized equations*

After spatial discretization the coupled set of nonlinear equations still has the form of (2.19). Terms on the right-hand side, which involve upstream interpolation, are first evaluated. The coupled set is rewritten as a linear one (where the coefficients depend on the basic state), plus a nonlinear perturbation, which is placed on the right-hand side and which is relatively cheap to evaluate. The set is then solved iteratively using the linear terms as a kernel, and reevaluating the nonlinear terms on the right-hand side at each of the iterations using the most recent values.

The nonlinearity is due mostly to the logarithmic terms  $\ln p$  and  $\ln \theta$  in the governing equations. The logarithmic nonlinearity is the mildest one possible, and provided the reference state is chosen appropriately the fixed point iterations will converge. The convergence, and optimization, of the iterative scheme were analyzed in Côté and Staniforth (1988). Two iterations, the minimum for stability, have been found sufficient for practical convergence in all our work since (Côté and Staniforth 1990; Côté et al. 1993, 1998b). Note however that because of the outer iteration the total number of iterations (and evaluation of the nonlinear terms) is 4, giving a scheme that is more robust than recently proposed predictor-corrector-like schemes at the European Centre for Medium-Range Weather Forecasts (Cullen et al. 2000) and Météo-France (I. G. Gospodinov 2000, personal communication).

The linear set can be algebraically reduced to the solution of a 3D elliptic boundary value (EBV) problem from which the other variables are obtained by back-substitution. This EBV problem for  $P$  is vertically separable and it is solved efficiently with the same solver described in Côté et al. (1998b)—the nonhydrostatic factors require a simple renormalization of the separation constants. The nonseparability in the horizontal is due to the Coriolis terms on the rotated grid, which are  $O(f\Delta t)$ . The preconditioned conjugate gradient method used in Côté et al. (1998b) requires very few iterations to converge, and we can stop at a fixed and small number of iterations that diminish with diminishing equivalent height. The preconditioner is obtained by replacing  $\nabla_f^2$  by  $a_0 \nabla^2$ , with  $a_0$  taken as

$$a_0 = \text{minimax} \left( \frac{1}{1 + \tau^2 f^2} \right) = \frac{1}{2} \left( 1 + \frac{1}{1 + 4\tau^2 \Omega^2} \right). \quad (2.28)$$

The linearization and the derivation of the 3D EBV problem along with its vertical separation are outlined in appendix B. Performing a vertical separation in a separable 3D EBV problem, as in the present work, has the virtue that horizontal and vertical scales no longer mix, something that we speculate may have been a

source of the convergence difficulties reported in Skamarock et al. (1997) in the context of the solution of a nonseparable EBV problem. The direct solver adopted herein as a preconditioner for the horizontal 2D EBV problems that result from the vertical separation procedure has the virtue that it directly handles the strongest horizontal variations. Only a couple of iterations are then needed to accommodate the slowly varying nonseparable Coriolis terms that result from the use of a rotated lat–lon coordinate system. However these iterations can be avoided by simply handling the nonseparable Coriolis terms together with the nonlinear ones, and this strategy has been adopted in the model since submission of the present paper. It remains to be seen whether the rapid convergence, observed for hydrostatic and mildly nonhydrostatic flows, of the iterative methods adopted herein also holds for strongly nonhydrostatic ones.

**3. Results**

The nonhydrostatic version of the Global Environmental Multiscale (GEM) model has been tested with real-data cases both at low and high resolutions. The global case at low resolution is a sensitivity test to illustrate the closeness of the results of the nonhydrostatic and hydrostatic versions for the hydrostatic regime, and two mesoscale events at high resolution are used to provide a preliminary assessment of the accuracy of the nonhydrostatic version. The experimental configurations are summarized in Table 1, where the diffusion coefficient is that of horizontal Laplacian diffusion, the digital filter refers to that of Fillion et al. (1995), and the physical parameterizations are based on the Recherche en Prévision Numérique (RPN) Physics 3.6 package described in Mailhot et al. (1998) with appropriate modifications (summarized later) for mesoscale applications. In all the experiments,  $Z_T$  and  $Z_S$  are taken as 10 and 1000 hPa, respectively, and  $T^*$  is 200 K. As in Côté et al. (1998a), the variable-resolution strategy is used to hindcast the mesoscale events. Note also that all computations are performed on a NEC SX-4 supercomputer at 32-bit arithmetic precision, except that 64-bit precision is used to solve the elliptic boundary value problem associated with the implicit time discretization. The experiments are all initiated from hydrostatic initial conditions, and the supplementary fields needed for the nonhydrostatic experiments are computed as described in appendix C.

Details of the experiments are described in the following subsections. The Courant–Friedrichs–Levy (CFL) numbers for advection are defined locally as

$$\text{horizontal CFL number} \equiv \frac{\Delta t}{a \cos \theta} \max \left( \frac{|u|}{\Delta \lambda}, \frac{|v|}{\Delta \theta} \right),$$

and

$$\text{vertical CFL number} \equiv \Delta t \frac{|\dot{Z}|}{\Delta Z},$$

TABLE 1. Model configurations for the global, suete and VORTEX cases.

Case	Global	Suete	VORTEX
Horizontal resolution	2° uniform	0.02° variable	0.04° variable
Vertical resolution	28 levels	35 levels	35 levels
Time step size	60 min	1 min	1 min
Integration period	48 h	12 h	18 h
Poles of computational mesh	Rotated	Rotated	Rotated
Digital filter span	6 h	Off	3 h
Diffusion coefficient	Zero	500 m <sup>2</sup> /s <sup>-1</sup>	500 m <sup>2</sup> /s <sup>-1</sup>
Sponge layer	Vertical	None	None
Off-centering coefficient ( $\epsilon$ )	Zero	0.1	0.1
Topography	Off/on	On	On
Physics	Off/full	Partial	Partial

where  $u$ ,  $v$ , and  $\dot{Z}$  are the  $\lambda$ ,  $\theta$ , and  $Z$  components of the wind, respectively. Unless otherwise mentioned, the poles and the equator refer to those of the computational mesh rather than those of the geographical system.

#### a. The global case

The hydrostatic assumption is globally considered to be well respected for scales larger than 10 km, and nonhydrostatic effects are negligible for scales larger than 100 km (e.g., Gill 1982). A global low-resolution experiment is thus conducted to test how close the forecasts of the two versions are for large- and synoptic-scale flow. As summarized in Table 1, the global sensitivity test is conducted with a uniform resolution of 2° in both the zonal and meridional directions, and with the 28 vertical levels of the operational configuration. The poles of the computational mesh are rotated with respect to the geographical ones, and are located in areas where the winds are climatologically relatively uniform in order to minimize the differences in the vicinity of the numerical poles. The initial atmosphere is obtained via an interpolation of a 16-level Canadian Meteorological Centre (CMC) isobaric analysis on a 400-point  $\times$  200-point latitude–longitude grid, valid at 0000 UTC 19 July 1996. A digital filter is employed to control high-frequency oscillations with periods shorter than 6 h. A large time step of 1 h is chosen such that the maximum horizontal CFL number is about 2 around the equator of the computational mesh, while the maximum vertical CFL number is much less than 1 for this case. The total integration time is 48 h. The horizontal diffusion is turned off in order to better highlight the differences between the hydrostatic and nonhydrostatic forecasts. These differences are summarized in Table 2,

where “plain dynamics” refers to the experiment without physics and topography, and “physics and topography” refers to the experiment described below with physics and topography included.

The nonhydrostatic version of the GEM model is first tested without physics and topography, and the same configuration is used to produce the hydrostatic control. The 24-h 500-hPa height difference statistics of the nonhydrostatic and hydrostatic forecasts are displayed in Table 2. The rms difference is 0.012 m, and the maximum absolute (maxnorm) difference is only 0.037 m. The 24-h mean sea level pressure (MSLP) differences are also very small as seen in Table 2. The nonhydrostatic index ( $\mu$ ) at hour 24 is  $O(10^{-7})$  throughout the whole domain, indicating that the vertical acceleration is extremely weak and that nonhydrostatic effects are indeed negligible for this case. The corresponding 48-h difference statistics (see Table 2) are very similar to the 24-h ones, except that the magnitudes are generally larger.

The sensitivity in the presence of both physics and topography is also examined. The full package of operational physical parameterizations is used for both the hydrostatic and nonhydrostatic integrations, and statistics of the differences are summarized in Table 2. The 24-h 500-hPa rms height difference is 0.284 m, while the maximum difference is 2.378 m, and the average difference is only  $-0.016$  m. The 24-h MSLP rms difference is 0.036 hPa, while the maximum absolute difference is only 0.251 hPa, and the bias is negligible. The 48-h differences (see Table 2) are generally of the same order of magnitude but somewhat larger.

The above results may be compared to those of a predecessor of the Canadian Mesoscale Compressible Community model (MC2; Tanguay et al. 1990), where the test was carried out without topography but with simple

TABLE 2. Statistics of the global sensitivity test.

Difference statistics	Plain dynamics			Physics and topography		
	Maxnorm	Avg	Rms	Maxnorm	Avg	Rms
24-h 500-hPa height (m)	0.037	-0.010	0.012	2.378	-0.016	0.284
48-h 500-hPa height (m)	0.178	-0.019	0.022	4.944	-0.015	0.427
24-h MSLP (hPa)	0.031	0.000	0.002	0.251	0.000	0.036
48-h MSLP (hPa)	0.032	0.000	0.003	0.314	0.000	0.056

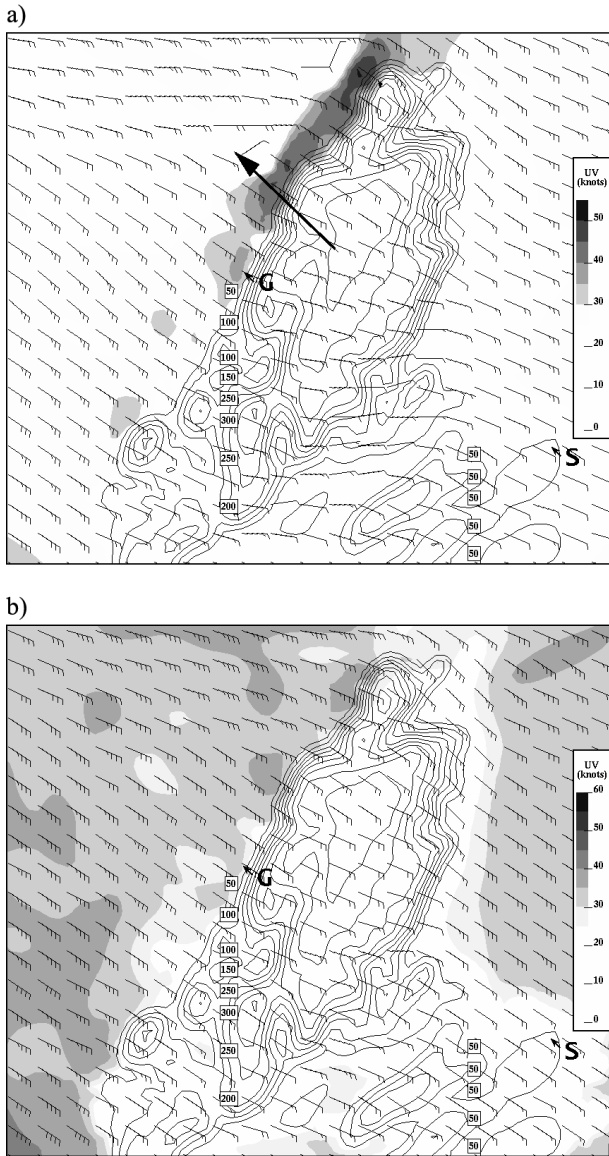


FIG. 1. (a) The 10-m wind valid at 0000 UTC 22 Dec 1993, as simulated by the nonhydrostatic GEM model after 6 h of integration; wind barbs (full, 10 kt; half, 5 kt) at approximately every 10 km. Winds exceeding 30 kt are shaded (interval 5 kt). The orography is contoured every 50 m. Sydney is marked with S; Grand-Étang is marked with G. (b) Same as in (a) except valid at 0300 UTC 22 Dec 1993 (9-h forecast).

physical parameterizations—a simple form of surface momentum, heat, and moisture fluxes, and a moist convective adjustment. It was reported in Tanguay et al. (1990) that the nonhydrostatic and hydrostatic forecasts for the 24-h 500-hPa height were identical up to three significant figures; that is, the difference was less than 10 m (how much less was not stated) compared to the 0.012-m difference reported herein. Note however that this was not an “identical twin” experiment since different vertical coordinates were employed in their hydrostatic and nonhydrostatic integrations. The GEM mod-

TABLE 3. The 35  $\eta$  levels for the suete and VORTEX cases.

0.0000	0.0097	0.0244	0.0448	0.0705
0.1007	0.1342	0.1695	0.2056	0.2444
0.2855	0.3284	0.3726	0.4175	0.4626
0.5076	0.5519	0.5952	0.6373	0.6779
0.7168	0.7530	0.7862	0.8165	0.8441
0.8691	0.8916	0.9118	0.9300	0.9462
0.9607	0.9736	0.9850	0.9950	1.000

el’s forecasts can also be compared to those presented in Qian et al. (1998), where an identical twin hydrostatic–nonhydrostatic experiment was carried out with topography but without physics. Those authors found that the maximum magnitude of the 48-h 500-hPa height difference between the nonhydrostatic and the hydrostatic forecasts was greater than 15 m (their Fig. 17c) compared to the 5-m difference observed herein.

The above initial analysis used by the GEM model was arbitrarily chosen from the CMC archives, and similar results were obtained in tests with other randomly chosen analyses. When tests were repeated using much larger time steps, for example, 2 or 3 h, in order to test the stability of the nonhydrostatic version, the only impact was a gradual increase in the differences due to increasing time-truncation error. It is concluded that the nonhydrostatic dynamics of the GEM model for large- and synoptic-scale flow is very close to the hydrostatic dynamics, confirming that running a global nonhydrostatic model for hydrostatic-scale flows does not introduce a spurious nonhydrostatic response.

*b. The suete case*

The suete case is a small-scale downslope wind event that occurs regularly on the western side of the Cape Breton Highlands, Nova Scotia, Canada. It was studied in Benoit et al. (1997) using the Canadian MC2 model, and in Côté et al. (1998a) using the hydrostatic version of the GEM model. Both studies concluded that the dynamics of this mild windstorm was dominated by the orographic forcing, and that nonhydrostatic effects were relatively unimportant. It is thus considered to be a good test of the dynamical balance of a nonhydrostatic model at high resolution.

Both hydrostatic and nonhydrostatic hindcasts of the suete event described in Côté et al. (1998a) are presented here using the experimental configuration summarized in Table 1. It has been found that this particular event is not very sensitive to the number of vertical levels nor to the precise value of the horizontal diffusion coefficient. In Côté et al. (1998a), the operational configuration of 28 levels and a horizontal diffusion coefficient of 2500 m<sup>2</sup> s<sup>-1</sup> were adopted to facilitate comparison with the Benoit et al. (1997) simulations. Here, however, these parameters have been changed to be the same as for the Verification of the Origins of Rotation in Tornadoes Experiment case presented in the following subsection, which has 35 levels (shown in Table 3) and a five-times-

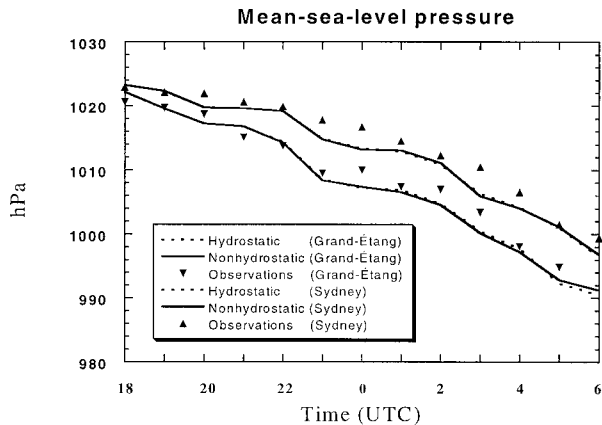


FIG. 2. Time series of MSLP at Sydney and Grand-Étang: nonhydrostatic forecasts (solid curves), hydrostatic forecasts (dashed curves), and observations (Sydney, upward pointing triangles; Grand-Étang, downward pointing triangles).

smaller diffusion coefficient of  $500 \text{ m}^2 \text{ s}^{-1}$ . All other configuration parameters are identical to those of Côté et al. (1998a). The GEM model's orography, initial analysis, and rotated variable-resolution mesh are, respectively, shown in Figs. 12, 13a, and 15 of Côté et al. (1998a). The horizontal resolution is  $0.02^\circ$  in the central domain with each successive mesh length increasing by 10% in each of the four coordinate directions when moving away from this high-resolution subdomain. The initial atmosphere, valid at 1800 UTC 21 December 1993, is obtained via interpolation from a 15-level isobaric analysis defined on a  $360\text{-point} \times 180\text{-point}$  Gaussian grid. Physical parameterizations are as in the Côté et al. (1998a) integration: no gravity wave drag, no convection, and simple condensation instead of the Sundqvist parameterization. The total integration time is 12 h with a 1-min time step. The maximum horizontal CFL number in the central domain is about 2.0 and the maximum vertical CFL number is about 1.5 during both the hydrostatic and nonhydrostatic integrations.

The 6-h 10-m wind forecast for the nonhydrostatic

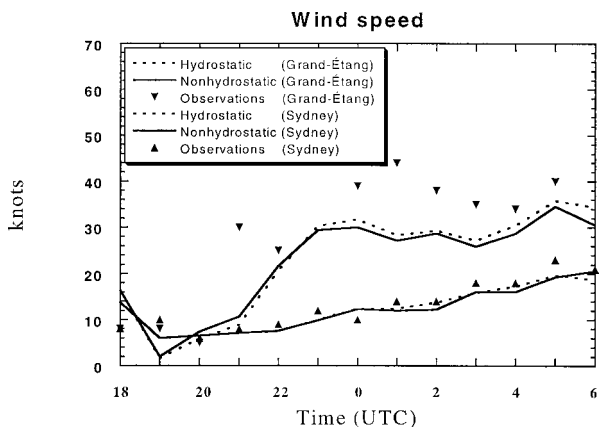


FIG. 3. Same as in Fig. 2 but for the surface (10 m) wind.

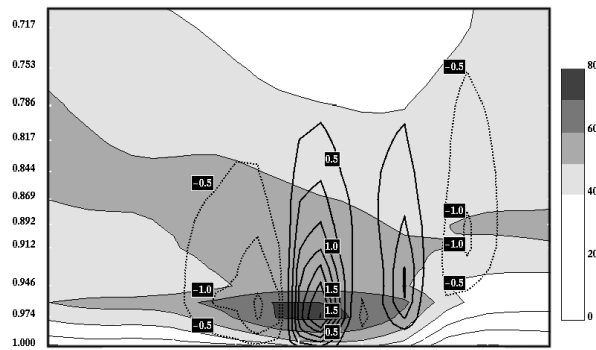


FIG. 4. Vertical cross section along the arrow plotted in Fig. 1a of the dimensionless nonhydrostatic index ( $\mu$ ) and the wind speed. Here,  $\mu$  is contoured in light lines, dotted negative, with contours at  $\pm(0.5, 1.0, 1.5, \dots) \times 10^{-3}$ ; winds exceeding 40 kt are shaded (interval 10 kt); the ordinate is  $\eta$ .

configuration of the GEM model is presented in Fig. 1a, where the orography is contoured every 50 m, the upstream station in Sydney is marked with S, and the station in Grand-Étang is marked with G. A strong downslope wind occurs on the lee side immediately offshore while the surrounding winds are weaker. The 9-h forecast, Fig. 1b, is shown for comparison with Benoit et al. (1997) and Côté et al. (1998a). The wind at this time however is more uniform over the whole region. The hydrostatic forecast (not shown) is very close to the nonhydrostatic one, consistent with the findings of the aforementioned studies.

The MSLP and surface wind forecasts of both the hydrostatic and nonhydrostatic configurations have been compared to observations at the (upstream) Sydney and (downstream) Grand-Étang stations, and time series are presented in Figs. 2 and 3, respectively. The nonhydrostatic MSLP (Fig. 2) forecasts (solid curves) are barely distinguishable from the hydrostatic ones (dashed curves), and all agree quite well with the observations

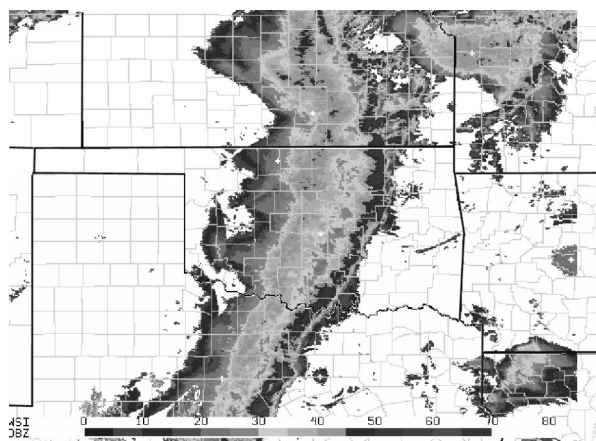


FIG. 5. The 1.5-km-altitude composite radar reflectivity image (dBZ) valid at 0200 UTC 8 May 1995, over Oklahoma and neighboring states.



FIG. 6. The  $353 \times 415$ -point grid used for the VORTEX case with a  $240 \times 323$ -point uniform resolution ( $0.04^\circ$ ) window. For clarity every third point in each direction is plotted.

(black triangles). The time series of surface wind (Fig. 3) at the two stations show that the nonhydrostatic forecasts (solid curves) are very close to the hydrostatic ones (dashed curves). They also agree quite well with the observations at the upstream Sydney station, while at the downstream Grand-Étang station the agreement is not quite as good, due partially to the gustiness of the observed winds, something that the model does not properly represent.

To better understand why the nonhydrostatic forecast is so similar to the hydrostatic one, a vertical cross section of the nonhydrostatic index  $\mu$  at 6 h, across the mountain crest and along the arrow shown in Fig. 1a, is plotted in Fig. 4. It is seen that the nonhydrostatic index is for the most part confined to low levels ( $\eta \gg 0.95$ ) by the strong stratification of the flow, and thus nonhydrostatic effects are significantly suppressed. The wind speed is also displayed in Fig. 4, and the region of maximum wind speed is well correlated to the nonhydrostatic index.

This experiment demonstrates that the nonhydrostatic GEM dynamics can maintain proper hydrostatic balance in weakly nonhydrostatic situations. It also indicates that the model is capable of making a reasonable mesoscale

forecast despite the lack of a high-resolution initial analysis and adequate physical parameterizations.

### c. The VORTEX case

The Verification of the Origins of Rotation in Tornadoes Experiment (VORTEX) project was conducted during the springs of 1994 and 1995 with the primary purpose of testing a set of hypotheses concerning tornadogenesis and tornado dynamics (Rasmussen et al. 1994). Data were also collected that are suitable for the study of convective storm dynamics and the structure of features in the boundary layer prior to the onset of convection (Bluestein et al. 1998). One of the interesting events observed in the VORTEX project is a typical squall line that occurred on 7–8 May 1995, and which is referred to here as the VORTEX case for convenience. This case was first studied by Wang et al. (1996), further analyzed by Xue et al. (1998a), and simulated by Wang et al. (1998) with a nonhydrostatic model and by Xue et al. (1998b) by data assimilation. The present goal is to demonstrate the capability of the GEM model to forecast the positions of the mesoscale squall line and the associated precipitation patterns, despite the inadequa-

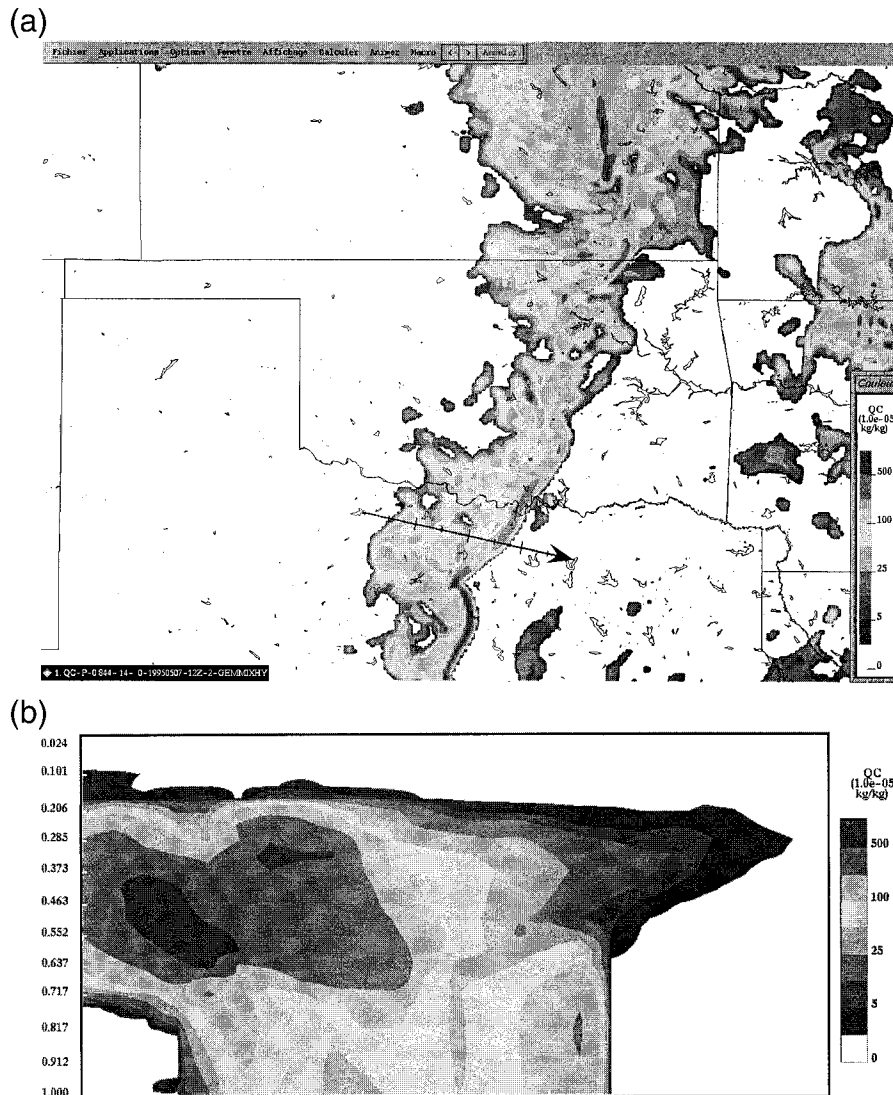


FIG. 7. (a) Specific total cloud water (including precipitation) at level  $\eta = 0.844$  for the 14-h hydrostatic forecast. Contours are at 1, 5, 10, 25, 50, 100, 250, and  $500 \times 10^{-5} \text{ kg kg}^{-1}$ . (b) Vertical cross section along the arrow plotted in (a) of the 14-h hydrostatic forecast of the specific total cloud water.

cies of a synoptic-scale initial analysis and the physical parameterizations employed.

At 1200 UTC 7 May 1995, a clearly defined dryline was observed along the New Mexico–Texas border. As it moved eastward into Texas, a band of convective clouds started to develop along the dryline around 1600 UTC, and more convective cells developed to the south of the dryline in western Texas within the next 2 h. The convection soon intensified and occurred along a line, which further evolved into a typical midlatitude squall line as it moved across the western border of Oklahoma around 2000 UTC. This squall line lasted more than 10 h and extended more than 1000 km in the south–north direction. Figure 5 shows the 1.5-km-altitude composite radar reflectivity image valid at 0200 UTC 8 May 1995,

when the squall line was at its mature stage with a solid leading convective edge and an associated trailing stratiform precipitation band parallel to the convective line. The cloud in the northeast sector of the major convective line corresponds to the tail of a relatively minor squall line formed a few hours earlier than the major one, and attention here is focused on the major squall line in central Oklahoma.

With the experimental configuration summarized in Table 1, both the hydrostatic and nonhydrostatic versions of the GEM model are used to simulate the squall line. The horizontal resolution is chosen to be  $0.04^\circ$  ( $\approx 4.4 \text{ km}$ ) so that the uniform high-resolution ( $240 \times 323$ -point) window of the  $353 \times 415$ -point mesh covers the evolution of the entire event. Figure 6 shows the

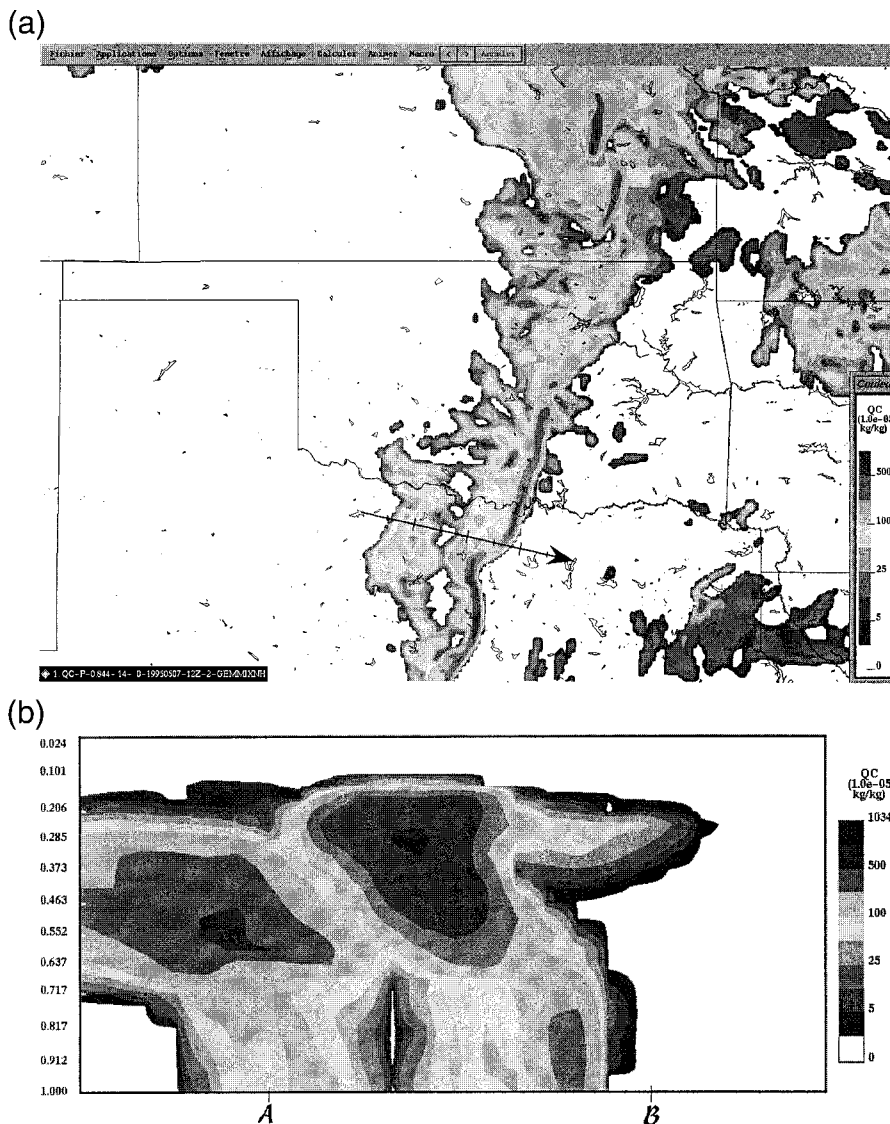


FIG. 8. (a) Same as in Fig. 7a but for the nonhydrostatic model. (b) Same as in Fig. 7b but for the nonhydrostatic model.

grid system of the GEM model for simulating this VORTEX case. The computational poles are rotated with respect to the geographical ones in order to center the uniform high-resolution window over the area of interest. The horizontal resolution is again smoothly degraded by the same 10% factor per successive mesh length when moving away from the uniform-resolution subdomain. Thirty-five vertical levels are adopted here, instead of the operational 28 levels, to better resolve the strong convection. The horizontal diffusion coefficient of  $500 \text{ m}^2 \text{ s}^{-1}$  is kept relatively small in order not to unduly smooth small-scale features. The total integration time is 18 h with a 1-min time step, and the maximum horizontal CFL number is about 2.0 in the central domain during both the hydrostatic and nonhydrostatic

integrations. The GEM model is initiated from an interpolation of a 21-level CMC analysis valid on a  $360 \times 180$ -point Gaussian grid at 1200 UTC 7 May 1995, when no convection was present along the dryline at the New Mexico–Texas border. The digital filter of Fillion et al. (1995) is employed for the model to reach dynamical balance with a cutoff frequency of 3 h. The physical parameterizations are based on the RPN Physics 3.6 package (Mailhot et al. 1998), but without the gravity wave drag and convective parameterizations that were designed for large-scale applications. For condensation, the mixed-phase cloud scheme of Tremblay et al. (1996) is used. The supercooled liquid water parameterization in this cloud scheme is turned off since its formulation is not appropriate for vertical motions stron-

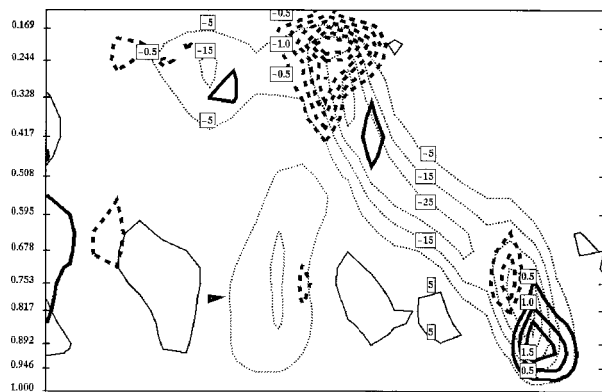


FIG. 9. Vertical cross section in the frontal region, between A and B in Fig. 8b of the 14-h nonhydrostatic forecast of the vertical motion ( $\omega \equiv dp/dt$ ) and the dimensionless nonhydrostatic index ( $\mu$ ). Here,  $\omega$  is contoured in light lines, dotted negative, with contours at  $\pm(5, 15, 25, \dots)$  Pa  $s^{-1}$ ;  $\mu$  is contoured in heavy lines, dotted negative, with contours at  $\pm(0.5, 1.0, 1.5, \dots) \times 10^{-3}$ .

ger than  $1 \text{ m s}^{-1}$ , and the strong convection in this case leads to vertical motion as strong as  $10 \text{ m s}^{-1}$ . The physical parameterizations are thus not adequate for fully simulating the precipitation, but are nevertheless adequate for testing the model dynamics. The 14-h forecasts are valid at 0200 UTC 8 May 1995, and the specific total cloud water (including precipitation) at the level  $\eta = 0.844$  is computed for subjective comparison with the observations shown in Fig. 5, which corresponds to precipitation at a height of approximately 1.5 km.

Figure 7a presents the 14-h hydrostatic forecast of the specific total cloud water at the level  $\eta = 0.844$ . The position of the hydrostatically forecast squall line is nearly perfect, although the convective line is slightly distorted in the middle section with relatively weak and scattered precipitation. Figure 7b shows a vertical cross section of the 14-h hydrostatic forecast of the total cloud water across the squall line, along the arrow plotted in Fig. 7a. The shape of the cloud (Fig. 7b) is reasonably well simulated with a prominent anvil in front of the convective line, although the cloud above the convective line is not quite connected to the cloud over the stratiform region.

Figure 8a shows the 14-h nonhydrostatic forecast of the total cloud water at the level  $\eta = 0.844$ , and Fig. 8b shows a vertical cross section across the squall line along the same arrow shown in both Figs. 7a and 8a. Comparing the nonhydrostatic forecast (Fig. 8a) to the observations (Fig. 5) and to the hydrostatic forecast (Fig. 7a), it is seen that the position of the forecasted squall line remains nearly perfect, and the slight distortion of the convective line in the middle section is improved in the nonhydrostatic simulation. The convection in the middle section of the nonhydrostatic simulation is stronger than that of the hydrostatic one, and the squall line is better defined in the nonhydrostatic simulation. In addition, the nonhydrostatic precipitation pattern (Fig. 8a) resembles the radar observations (Fig. 5) slightly better than the hydrostatic one (Fig. 7a) does,

with a better resolved stratiform precipitation band in the southern section of the squall line. The shape of the cloud is also improved in the nonhydrostatic simulation (Fig. 8b) inasmuch as the convective clouds are better connected and the stratiform region is more clearly separated from the convective line, reflecting a stronger inflow from the lower boundary in the nonhydrostatic integration. The simulated stratiform regions (Figs. 7a and 8a) are not as wide as in the observations (Fig. 5), which may be attributed to the coarse initial analysis and the inadequacies of the physical parameterizations.

Figure 9 presents a vertical cross section in the frontal region, between A and B of Fig. 8b of the 14-h nonhydrostatic forecast of the vertical motion ( $\omega \equiv dp/dt$ ) and the dimensionless nonhydrostatic index ( $\mu$ ). The mechanism that drives the eastward movement of the convective line is well illustrated with a shift of the maximum convection created by the upward acceleration immediately in front of the convective line, and downward acceleration right behind the convective line. During the integration the vertical acceleration ( $g\mu$ ) reaches a maximum absolute value of about  $0.1 \text{ m s}^{-2}$ , but the nonhydrostatic effects are however quite localized horizontally, being confined to areas of strong convection.

Finally, the maximum vertical CFL number is 2.7 during the nonhydrostatic integration, while the hydrostatic integration attains the much larger value of 6.1, indicating that the strong vertical wind is not properly treated by the hydrostatic dynamics.

#### 4. Conclusions

The hydrostatic formulation of Côté et al. (1998b) has been generalized to include nonhydrostatic effects using a terrain-following coordinate based on Laprise's (1992) hydrostatic pressure. The new version costs approximately 10% more than the hydrostatic one, and the efficiency in integrations performed to date is well maintained in the nonhydrostatic model by the use of the relatively large time steps permitted by the (almost) fully implicit semi-Lagrangian discretization.

Results indicate that for large- and synoptic-scale flow the nonhydrostatic dynamics of the GEM model is highly consistent with that of its hydrostatic subset. For mesoscale flows, the impact of representing nonhydrostatic effects is stronger, and appears physically realistic, despite some inadequacies of the physical parameterizations. The thoroughness of this assessment is however limited by the absence of verifying mesoscale analyses.

Development is continuing on the GEM forecasting system and, for example, the GEM model is now coupled to state-of-the-art microphysics packages, making it a powerful tool for mesoscale case studies in an operational context. Nevertheless much work remains to be done, particularly on rigorous testing of the model's performance for strongly nonhydrostatic flows. One aspect is model validation against known analytic or numerically converged solutions. Another is the model's

efficiency and robustness in the strongly nonhydrostatic regime. It remains to be demonstrated that sufficiently large time steps can be used to offset the possible increased cost (particularly in the presence of steep terrain) of iterating the Helmholtz solver and nonlinear terms to an adequate level of convergence—to accomplish this, thorough experimentation will need to be performed using a quantitative convergence measure.

*Acknowledgments.* The first author acknowledges the financial support of the Centre de Recherche en Calcul Appliqué, and the support of RPN's programming section.

Thanks are due to Dr. Stéphane Belair for providing the VORTEX data and for his advice on physical parametrizations, and to Yves Chartier for his expert final touch to the artwork. We are also indebted to Prof. René Laprise for many fruitful discussions in the initial phase of this project.

## APPENDIX A

### Spatial Discretization

#### *a. Horizontal discretization and finite-differencing*

The scalar grid, the set of points where the scalar fields are defined, is described by giving a list of longitudes ( $\lambda$ ) and a list of latitudes ( $\theta$ ), of size NI and NJ, respectively. Thus

$$\{(\lambda_i, \theta_j), i = 1, \text{NI}; j = 1, \text{NJ}\}. \quad (\text{A.1})$$

The grid points satisfy the constraints

$$0 \leq \lambda_i < 2\pi, \quad \lambda_1 = 0, \quad -\frac{\pi}{2} < \theta_j < \frac{\pi}{2}. \quad (\text{A.2})$$

Note that the poles do not belong to the scalar grid. It is convenient to introduce the grid extensions

$$\begin{aligned} \lambda_0 &= \lambda_{\text{NI}} - 2\pi, & \lambda_{\text{NI}+1} &= \lambda_1 + 2\pi \\ \theta_0 &= -\frac{\pi}{2}, & \theta_{\text{NJ}+1} &= \frac{\pi}{2}, \end{aligned} \quad (\text{A.3})$$

and grid differences

$$\begin{aligned} \Delta\lambda_i &= \lambda_{i+1} - \lambda_i, & i &= 0, \text{NI}, & (\Delta\lambda_0 &= \Delta\lambda_{\text{NI}}) \\ \Delta\sin\theta_j &= \sin\theta_{j+1} - \sin\theta_j, & j &= 0, \text{NJ}. \end{aligned} \quad (\text{A.4})$$

The grid points of the zonal wind image ( $U$ ) are located at the same latitudes as the scalar grid points but at longitudes situated halfway between those of the scalar grid. Thus

$$\begin{aligned} \{(\tilde{\lambda}_i, \theta_j), i = 1, \text{NI}; j = 1, \text{NJ}\} \\ \tilde{\lambda}_i &= \frac{(\lambda_i + \lambda_{i+1})}{2}, & i &= 1, \text{NI}. \end{aligned} \quad (\text{A.5})$$

An extension and differences are also introduced for the  $U$  grid:

$$\begin{aligned} \tilde{\lambda}_0 &= \tilde{\lambda}_{\text{NI}} - 2\pi, & \tilde{\lambda}_{\text{NI}+1} &= \tilde{\lambda}_1 + 2\pi \\ \Delta\tilde{\lambda}_i &= \tilde{\lambda}_{i+1} - \tilde{\lambda}_i, & i &= 0, \text{NI}. \end{aligned} \quad (\text{A.6})$$

The grid points of the meridional wind image ( $V$ ) are located at the same longitudes as the scalar grid points but at latitudes situated halfway between those of the scalar grid. Thus

$$\begin{aligned} \{(\lambda_i, \tilde{\theta}_j), i = 1, \text{NI}; j = 1, \text{NJ} - 1\} \\ \tilde{\theta}_j &= \frac{(\theta_j + \theta_{j+1})}{2}, & j &= 1, \text{NJ} - 1. \end{aligned} \quad (\text{A.7})$$

An extension and differences are similarly introduced for the  $V$  grid:

$$\begin{aligned} \tilde{\theta}_0 &= -\frac{\pi}{2}, & \tilde{\theta}_{\text{NJ}} &= \frac{\pi}{2} \\ \Delta\sin\tilde{\theta}_j &= \sin\tilde{\theta}_{j+1} - \sin\tilde{\theta}_j, & j &= 0, \text{NJ} - 1. \end{aligned} \quad (\text{A.8})$$

Note that the wind images both vanish at the poles, and we do not need to carry them there.

The images of the gradient vector of a scalar field  $\phi$  are given by

$$\frac{\cos\theta}{a} \nabla\phi = \frac{1}{a^2} \left( \frac{\partial\phi}{\partial\lambda} \hat{\mathbf{e}}_\lambda + \cos^2\theta \frac{\partial\phi}{\partial\sin\theta} \hat{\mathbf{e}}_\theta \right), \quad (\text{A.9})$$

and each component is computed with a centered difference. This gives for the zonal direction

$$\left. \frac{\partial\phi}{\partial\lambda} \right|_{i,j} = \frac{\phi_{i+1,j} - \phi_{i,j}}{\Delta\lambda_i}, \quad (\phi_{\text{NI}+1,j} \equiv \phi_{1,j}), \quad (\text{A.10})$$

where the result is on the  $U$  grid, likewise for the meridional direction

$$\cos^2\theta \left. \frac{\partial\phi}{\partial\sin\theta} \right|_{i,j} = \cos^2\tilde{\theta}_j \frac{\phi_{i,j+1} - \phi_{i,j}}{\Delta\sin\tilde{\theta}_j}, \quad (\text{A.11})$$

the result being on the  $V$  grid.

The horizontal divergence of the wind is given by

$$D = \nabla \cdot \mathbf{V}^H = \frac{1}{\cos^2\theta} \frac{\partial U}{\partial\lambda} + \frac{\partial V}{\partial\sin\theta} \quad (\text{A.12})$$

and is computed as

$$\begin{aligned} D_{ij} &= \frac{1}{\cos^2\theta_j} \frac{U_{i,j} - U_{i-1,j}}{\Delta\tilde{\lambda}_{i-1}} + \frac{V_{i,j} - V_{i,j-1}}{\Delta\sin\tilde{\theta}_{j-1}}, \\ (U_{0,j} &\equiv U_{\text{NI},j}, V_{i,0}, V_{i,\text{NJ}} \equiv 0), \end{aligned} \quad (\text{A.13})$$

which is centered in the case of a uniform grid and in the uniform portion of a variable grid.

To compute the horizontal Laplacian of the scalar  $\phi$

$$R = a^2 \nabla^2 \phi, \quad (\text{A.14})$$

the discrete gradient and divergence operators are applied on  $\phi$  in succession giving

$$\mathbf{P}_{(\theta)} \otimes \mathbf{P}_{(\lambda)} R = [\mathbf{P}'_{(\theta)} \otimes \mathbf{P}_{\lambda\lambda} + \mathbf{P}_{\theta\theta} \otimes \mathbf{P}_{(\lambda)}] \phi, \quad (\text{A.15})$$

where





$$\frac{(\phi - \phi^*)}{\tau} - R_d T^* \frac{\dot{Z}}{Z} - gw = R^w, \quad \frac{\delta_H w}{\tau} - g\tau \frac{\partial Q}{\partial Z} = (R - N)^v; \quad (\text{B.11})$$

(B.1)

where  $\tau = (1 + 2\varepsilon)\Delta t/2$ .

First,  $\phi$  is split into a reference part plus a perturbation:

$$\phi = \phi^*(Z) + \phi_s + \phi'. \quad (\text{B.2})$$

Linearization then proceeds with respect to the following set of variables:

$$\phi', \mathbf{V}^H, w, \dot{Z}', s, q'. \quad (\text{B.3})$$

For example, the variables  $T_v$ ,  $\pi$ , and  $\mu$  are expanded as

$$T_v = T^* + T' + \dots, \quad \pi = Z + \pi' + \dots \\ \mu = 0 + \mu' + \dots \quad (\text{B.4})$$

It is convenient to introduce the following auxiliary variables:

$$P = \phi' + R_d T^* \left( \frac{\pi'}{Z} + q' \right), \quad X = \frac{\pi'}{\tau} + \dot{Z} \\ Q = \frac{Z}{\tau} q', \quad (\text{B.5})$$

from which we obtain

$$T' = -\frac{1}{R_d} LP + T^* \tau \frac{\partial Q}{\partial Z}, \quad \pi' = (Z - Z_T) s \\ \mu' = \tau \frac{\partial Q}{\partial Z}, \quad (\text{B.6})$$

where

$$L = \frac{\partial}{\partial \ln Z} = Z \frac{\partial}{\partial Z}. \quad (\text{B.7})$$

Next the nonlinear contributions to the left-hand sides of the prognostic equations are evaluated using the most recent values and put on the right-hand sides along with contributions of known fields, such as  $\phi_s$ , yielding the following:

*linearized horizontal momentum and divergence equations,*

$$\frac{\mathbf{V}^H}{\tau} + \nabla P + f(\mathbf{k} \times \mathbf{V}^H) = (\mathbf{R}' - \mathbf{N})^H \Rightarrow \frac{D}{\tau} + \nabla_f^2 P \\ = (R' - N)^D; \quad (\text{B.8})$$

*continuity equation,*

$$\frac{\partial X}{\partial Z} + D = R^C; \quad (\text{B.9})$$

*linearized thermodynamic equation,*

$$-\frac{1}{R_d T^* \tau} LP - \frac{\kappa}{Z}(X + Q) + \frac{\partial Q}{\partial Z} = (R - N)^0; \quad (\text{B.10})$$

*linearized vertical momentum equation,*

*vertical velocity equation,*

$$\frac{1}{g\tau} P - \frac{R_d T^*}{Z}(X + Q) - gw = R'^w. \quad (\text{B.12})$$

In the above  $\nabla_f^2$  is the modified Laplacian (A.20),  $N$  denotes the nonlinear contributions from the left-hand side,  $R'$  shows that a contribution from  $\phi_s$  has been subtracted out, and  $\mu \nabla \phi$  is treated as a purely nonlinear term.

An elliptic boundary value problem for  $P$  is obtained by eliminating all of the other variables from (B.8) to (B.12) as follows. Eliminating  $D$  between the divergence and continuity equations (B.8) and (B.9) gives

$$\nabla_f^2 P - \frac{1}{\tau} \frac{\partial X}{\partial Z} = R_1, \quad (\text{B.13})$$

and eliminating  $w$  from the linearized vertical momentum and vertical velocity equations (B.11) and (B.12) yields

$$\frac{\delta_H}{g^2 \tau^3} P - \frac{\delta_H R_d T^*}{g^2 \tau^2 Z}(X + Q) - \frac{\partial Q}{\partial Z} = R_2. \quad (\text{B.14})$$

Eliminating  $\partial Q / \partial Z$  between (B.14) and the linearized thermodynamic equation (B.10) gives

$$\left( \frac{L}{\kappa R_d T^* \tau} - \frac{\delta_H}{\kappa g^2 \tau^3} \right) P + \frac{1}{\gamma Z}(X + Q) = R_3. \quad (\text{B.15})$$

Equation (B.15) is then used to eliminate  $X + Q$  from (B.14) to obtain

$$\frac{\delta_H}{g^2 \tau^3} \left( 1 + \frac{L}{\kappa} \right) P - \frac{1}{\gamma} \frac{\partial Q}{\partial Z} = R_4, \quad (\text{B.16})$$

where

$$\gamma^{-1} = 1 + \frac{\delta_H R_d T^*}{\kappa g^2 \tau^2}. \quad (\text{B.17})$$

Finally (B.13) +  $\gamma(L + 1)/\tau$ (B.15) +  $\gamma/\tau$ (B.16) yields

$$\left[ \nabla_f^2 - \frac{\delta_H \gamma (1 - \kappa)}{\kappa g^2 \tau^4} + \frac{\gamma L (L + 1)}{\kappa R_d T^* \tau^2} \right] P = R_5, \quad (\text{B.18})$$

which, using (A.22)–(A.24) is vertically discretized as

$$\left\{ \left[ \nabla_f^2 - \frac{\delta_H \gamma (1 - \kappa)}{\kappa g^2 \tau^4} \right] \mathbf{V}(Z) + \frac{\gamma}{\kappa R_d T^* \tau^2} \mathbf{V}_{ZZ} \right\} P = \mathbf{R}^H. \quad (\text{B.19})$$

Equation (B.19) is easily decoupled as a set of horizontal problems using the solution of the following auxiliary generalized eigenvalue problem,

$$\mathbf{V}_{ZZ} \psi_k = \varepsilon_k \mathbf{V}(Z) \psi_k, \quad k = 1, NK, \quad (\text{B.20})$$

and the expansion

$$P(\lambda, \theta, Z_k) = \sum_{k'=1, NK} P_{k'}(\lambda, \theta) \psi_{k'}(Z_k). \quad (\text{B.21})$$

APPENDIX C

Vertical Velocities at Initial Time

The computation of the vertical velocities at initial time is given here. The model requires the two vertical velocities  $\dot{Z}$  and  $w$ . As usual  $\dot{Z}$  is obtained by vertically integrating the continuity equation (2.7) using the boundary conditions (2.15). To obtain  $w$ , assume that the integration starts from an hydrostatic and adiabatic state.

Kasahara's (1974) form of the continuity equation in the present generalized vertical coordinate gives

$$\frac{\partial}{\partial t} \left( \rho \frac{\partial \phi}{\partial Z} \right) + \nabla \cdot \left( \rho \mathbf{V} \frac{\partial \phi}{\partial Z} \right) + \frac{\partial}{\partial Z} \left( \rho \dot{Z} \frac{\partial \phi}{\partial Z} \right) = 0. \quad (\text{C.1})$$

and, dividing by  $\rho$ , this can be rewritten as

$$\frac{\partial \phi}{\partial Z} \frac{d \ln \rho}{dt} + \nabla \cdot \left( \frac{\partial \phi}{\partial Z} \mathbf{V} \right) + \frac{\partial}{\partial Z} \left( \frac{\partial \phi}{\partial t} + \dot{Z} \frac{\partial \phi}{\partial Z} \right) = 0. \quad (\text{C.2})$$

Integrating (C.2) from  $Z$  to  $Z_s$ , and using

$$\left( \frac{\partial \phi}{\partial Z} + \dot{Z} \frac{\partial \phi}{\partial Z} \right) \equiv \frac{d\phi}{dt} - \mathbf{V} \cdot \nabla \phi, \quad (\text{C.3})$$

leads to

$$\begin{aligned} \frac{d\phi}{dt} &\equiv gw \\ &= \mathbf{V} \cdot \nabla \phi - \int_{Z_s}^Z \left[ \frac{\partial \phi}{\partial Z'} \frac{d \ln \rho}{dt} + \nabla \cdot \left( \frac{\partial \phi}{\partial Z'} \mathbf{V} \right) \right] dZ'. \end{aligned} \quad (\text{C.4})$$

For hydrostatic and adiabatic motion,

$$\frac{d \ln \rho}{dt} = (1 - \kappa) \frac{d \ln \pi}{dt} = (1 - \kappa) \frac{\dot{\pi}}{\pi}, \quad (\text{C.5})$$

where

$$\dot{\pi} = \frac{\partial \pi}{\partial Z} \dot{Z} + \frac{\partial \pi}{\partial s} \dot{s} = \exp(s) \dot{Z} + (\pi - \pi_T) \dot{s}. \quad (\text{C.6})$$

Now from (2.7)

$$\dot{s} + D + \frac{\partial \dot{Z}}{\partial Z} = \frac{\partial s}{\partial t} + \mathbf{V} \cdot \nabla_s + D + \frac{\partial \dot{Z}}{\partial Z} = 0, \quad (\text{C.7})$$

which is integrated again from  $Z$  to  $Z_s$ , making use of the boundary condition (2.15) at the surface, to give

$$\dot{Z} = \int_Z^{Z_s} \left( \frac{\partial s}{\partial t} + \mathbf{V} \cdot \nabla_s + D \right) dZ'. \quad (\text{C.8})$$

Evaluating (C.8) at the top and applying boundary condition (2.15) then leads to

$$\frac{\partial s}{\partial t} = \frac{1}{(Z_s - Z_T)} \int_{Z_s}^{Z_T} (\mathbf{V} \cdot \nabla_s + D) dZ' \quad \text{and} \quad (\text{C.9})$$

$$\dot{s} = \mathbf{V} \cdot \nabla_s + \frac{1}{(Z_s - Z_T)} \int_{Z_s}^{Z_T} (\mathbf{V} \cdot \nabla_s + D) dZ'. \quad (\text{C.10})$$

Inserting (C.9) into (C.8) gives

$$\begin{aligned} \dot{Z} &= \int_Z^{Z_s} (\mathbf{V} \cdot \nabla_s + D) dZ' \\ &\quad - \frac{(Z_s - Z)}{(Z_s - Z_T)} \int_{Z_T}^{Z_s} (\mathbf{V} \cdot \nabla_s + D) dZ', \end{aligned} \quad (\text{C.11})$$

from which  $w$  can be computed by backsubstituting (C.10) and (C.11) into (C.6), then (C.6) into (C.5), and finally (C.5) into (C.4).

REFERENCES

Benoit, R., M. Desgagné, P. Pellerin, S. Pellerin, Y. Chartier, and S. Desjardins, 1997: The Canadian MC2: A semi-Lagrangian, semi-implicit wideband atmospheric model suited for finescale process studies and simulation. *Mon. Wea. Rev.*, **125**, 2382–2415.

Bluestein, H. B., E. Rasmussen, R. Davies-Jones, R. Wakimoto, and M. L. Weisman, 1998: VORTEX Workshop Summary, 2–3 December 1997, Pacific Grove, California. *Bull. Amer. Meteor. Soc.*, **79**, 1397–1400.

Bubnova, R., G. Hello, P. Bénard, and J.-F. Geleyn, 1994: An efficient alternative to z-coordinate for compressible flow over orography: Use of hydrostatic pressure as vertical coordinate in a complete NWP mesoscale model. Preprints, *10th Conf. on Numerical Weather Prediction*, Portland, OR, Amer. Meteor. Soc., 35–37.

—, —, —, and —, 1995: Integration of the fully elastic equations cast in hydrostatic pressure terrain-following coordinate in the framework of the ARPEGE/Aladin NWP system. *Mon. Wea. Rev.*, **123**, 515–535.

Côté, J., and A. Staniforth 1988: A two-time-level semi-Lagrangian semi-implicit scheme for spectral models. *Mon. Wea. Rev.*, **116**, 2003–2012.

—, and —, 1990: An accurate and efficient finite-element global model of the shallow-water equations. *Mon. Wea. Rev.*, **118**, 2707–2717.

—, M. Roch, A. Staniforth, and L. Fillion, 1993: A variable-resolution semi-Lagrangian finite-element global model of the shallow-water equations. *Mon. Wea. Rev.*, **121**, 231–243.

—, S. Gravel, M. Roch, A. Patoine, and A. Staniforth, 1994: A non-hydrostatic variable-resolution global model of the atmosphere. Preprints, *10th Conf. on Numerical Weather Prediction*, Portland, OR, Amer. Meteor. Soc., 171–172.

—, J.-G. Desmarais, S. Gravel, A. Méthot, A. Patoine, M. Roch, and A. Staniforth, 1998a: The operational CMC–MRB Global Environmental Multiscale (GEM) model. Part II: Results. *Mon. Wea. Rev.*, **126**, 1397–1418.

—, S. Gravel, A. Méthot, A. Patoine, M. Roch, and A. Staniforth, 1998b: The operational CMC–MRB Global Environmental Multiscale (GEM) model. Part I: Design considerations and formulation. *Mon. Wea. Rev.*, **126**, 1373–1395.

Cullen, M. J. P., D. Salmond, and P. Smolarkiewicz, 2000: Key numerical issues for the future development of the ECMWF numerical model. *Proc. ECMWF Workshop on Development in Numerical Methods for Very High Resolution Global Models*, Reading, United Kingdom, ECMWF, 183–206.

Daley, R. W., 1988: The normal modes of the spherical non-hydrostatic equations with applications to the filtering of acoustic modes. *Tellus*, **40A**, 96–106.

Fillion, L., H. L. Mitchell, H. Ritchie, and A. Staniforth, 1995: The

- impact of a digital filter finalization technique in a global data assimilation system. *Tellus*, **47A**, 304–323.
- Fox-Rabinovitz, M., G. Stenchikov, M. Suarez, and L. Takacs, 1997: A finite-difference GCM dynamical core with a variable resolution stretched grid. *Mon. Wea. Rev.*, **125**, 2943–2968.
- Gill, A. E., 1982. *Atmosphere–Ocean Dynamics*. Academic Press, 662 pp.
- Kasahara, A., 1974: Various vertical coordinate systems used for numerical weather prediction. *Mon. Wea. Rev.*, **102**, 509–522.
- Laprise, R., 1992: The Euler equations of motion with hydrostatic pressure as an independent variable. *Mon. Wea. Rev.*, **120**, 197–207.
- Mailhot, J., and Coauthors, 1998: Scientific description of RPN Physics Library. Version 3.6. Recherche en Prévision Numérique, 188 pp. [Available online at <http://www.cmc.ec.gc.ca/rpn/physics/physic98.pdf>.]
- Phillips, N. A., 1957: A coordinate system having some special advantages for numerical forecasting. *J. Meteor.*, **14**, 184–185.
- Qian, J.-H., F. H. M. Semazzi, and J. S. Scroggs, 1998: A global nonhydrostatic semi-Lagrangian atmospheric model with topography. *Mon. Wea. Rev.*, **126**, 747–771.
- Rasmussen, E. N., J. M. Straka, R. Davies-Jones, C. A. Doswell III, F. H. Carr, M. D. Eilts, and D. R. MacGorman, 1994: Verification of the Origins of Rotation in Tornadoes Experiment: VORTEX. *Bull. Amer. Meteor. Soc.*, **75**, 995–1006.
- Rivest, C., A. Staniforth, and A. Robert, 1994: Spurious resonant response of semi-Lagrangian discretizations to orographic forcing: Diagnosis and solution. *Mon. Wea. Rev.*, **122**, 366–376.
- Skamarock, W. C., P. K. Smolarkiewicz, and J. B. Klemp, 1997: Preconditioned conjugate-residual solvers for Helmholtz equations in nonhydrostatic models. *Mon. Wea. Rev.*, **125**, 587–599.
- Tanguay, M., A. Simard, and A. Staniforth, 1989: A three-dimensional semi-Lagrangian scheme for the Canadian regional finite-element forecast model. *Mon. Wea. Rev.*, **117**, 1861–1871.
- , A. Robert, and R. Laprise, 1990: A semi-implicit semi-Lagrangian fully compressible regional forecast model. *Mon. Wea. Rev.*, **118**, 1970–1980.
- Tremblay, A., A. Glazer, W. Yu, and R. Benoit, 1996: A mixed-phase cloud scheme based on a single prognostic equation. *Tellus*, **48A**, 483–500.
- Wang, D., M. Xue, V. Wong, and K. K. Droegemeier, 1996: Prediction and simulation of convective storms during VORTEX 95. Preprints, *11th Conf. on Numerical Weather Prediction*, Norfolk, VA, Amer. Meteor. Soc., 301–303.
- , —, D. Hou, and K. K. Droegemeier, 1998: Midlatitude squall line propagation and structure as simulated by a 3D nonhydrostatic stormscale model. Preprints, *12th Conf. on Numerical Weather Prediction*, Phoenix, AZ, Amer. Meteor. Soc., 209–212.
- Xue, M., D. Hou, D. Wang, and K. K. Droegemeier, 1998a: Analysis and prediction of convective initiation along a dryline. Preprints, *16th Conf. on Weather Analysis and Forecasting*, Phoenix, AZ, Amer. Meteor. Soc., 161–163.
- , D. Wang, D. Hou, K. Brewster, and K. K. Droegemeier, 1998b: Prediction of the 7 May 1995 squall lines over the central U.S. with intermittent data assimilation. Preprints, *12th Conf. on Numerical Weather Prediction*, Phoenix, AZ, Amer. Meteor. Soc., 191–194.
- Yanenko, N. N., 1971: *The Method of Fractional Steps*. Springer, 160 pp.